IEEE Photonics Journal
An IEEE Photonics Society Publication

Theoretical Investigation of a Plasmonic Demultiplexer in MIM Waveguide Crossing with Multiple Side-Coupled Hexagonal Resonators

Volume 8, Number 5, October 2016

Yi-Yuan Xie
Chao He
Jia-Chao Li
Ting-Ting Song
Zhen-Dong Zhang
Qian-Ren Mao

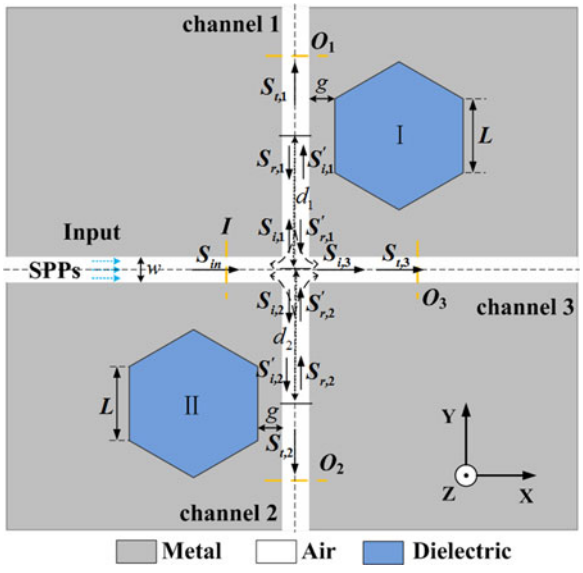

DOI: 10.1109/JPHOT.2016.2606319
1943-0655 © 2016 IEEE

Theoretical Investigation of a Plasmonic Demultiplexer in MIM Waveguide Crossing with Multiple Side-Coupled Hexagonal Resonators

Yi-Yuan Xie,[1,2] Chao He,[1] Jia-Chao Li,[1] Ting-Ting Song,[1] Zhen-Dong Zhang,[1] and Qian-Ren Mao[3]

[1]School of Electronic and Information Engineering, Southwest University, Chongqing 400715, China
[2]School of Optoelectronic Information, University of Electronic Science and Technology of Chengdu, Chengdu 611731, China
[3]College of Computer, China West Normal University, Nanchong 637009, China

DOI:10.1109/JPHOT.2016.2606319

Manuscript received July 20, 2016; revised August 24, 2016; accepted September 1, 2016. Date of publication September 13, 2016; date of current version September 20, 2016. This work was supported in part by the 863 program of China under Grant 2015AA016304, in part by the National Natural Science Foundation of China under Grant 61421002, in part by the National Natural Science Foundation of Chongqing City under Grant cstc2016jcyjA2002, in part by the Postdoctoral Science Foundation of China under Grant 2016M590875, and in part by the Fundamental Research Funds for the Central Universities under Grant XDJK2014A017 and Grant XDJK2016A011. Corresponding author: Y. Y. Xie (e-mail: yyxie@swu.edu.cn).

Abstract: A novel plasmonic demultiplexer in metal–insulator–metal (MIM) waveguide crossing with multiple side-coupled hexagonal resonators is proposed and numerically investigated. The operating principle of the structure is analyzed by using the temporal coupled-mode theory. It is found that wavelength demultiplexing can be realized by modulating locations of resonators, which is validated by finite-difference time-domain (FDTD) simulations. In addition, the influences of structural parameters on transmission characteristics are studied by simulations. Simulation results reveal that the demultiplexed wavelength, transmission efficiency, and bandwidth of each channel can be manipulated by adjusting structural parameters of the demultiplexer. The proposed demultiplexer will provide an alternative for the design of highly integrated optical circuits and complex waveguide networks.

Index Terms: Hexagonal resonator, metal-insulator-metal (MIM) waveguide, surface plasmon polaritons, waveguide crossing, wavelength demultiplexing.

1. Introduction

The previous couple of years have witnessed the prevalence of studies on nanophotonics based on surface plasmon polaritons (SPPs) [1]–[4]. Because of their unique capacity to conquer the diffraction limit and guide light at the nanoscale, SPPs are considered as promising energies and information carriers for realizing highly integrated photonic information processing systems [1], [5], [6]. Thus far, various optical devices based on SPPs have been proposed and investigated numerically or experimentally [7]–[11]. Among these devices, those made of metal-insulator-metal (MIM) waveguide which consists of a dielectric core and two metallic overlying layers have attracted

special research interests [12], [13]. A variety of components associated with MIM waveguide have been designed, for example, filters [14], [15]; slow light waveguides [16]; all-optical switches [17]; sensors [18], [19]; splitters [20]; and demultiplexers [21]–[24]. These results greatly promote the miniaturization and functionality of plasmonic waveguide structures. However, in constructing highly integrated optical circuits, the ability to intersect waveguides is also noteworthy to complex systems involving multiple waveguides [25], such as complex optical system [26]; resonant guided wave networks [27], [28]; big data center networks [29]; and optical networks-on-chips [30].

In recent years, researchers have done some studies on crossed waveguide structures. In earlier work, SPPs waves at intersection have been shown to be uniformly split into each output branch [27], [31]. To modify power distribution in each branch, some new configurations were proposed. For example, square ring resonators were introduced to the T-shaped bend and cross intersection to realize plasmon flow control [32]. By utilizing Fabry-Perot (FP) cavities, slot cavities [33]; and loop-based resonators [34], combined with four drop waveguides, the crosstalk was suppressed, and the forward transmittance was improved; moreover, these two structures can be implemented wavelength filtering. The wavelength demultiplexer based on waveguide crossing, which can transmit specific wavelengths into different branches in cross structure, is worthy of attention. However, we find that detailed research of such structure is rare. Liu *et al.* [35] and Lu *et al.* [36] have proposed demultiplexing structures in MIM waveguide crossing by using side-coupled rectangular resonators and nanodisk resonators, but they were based on a dual band-stop filter to design them. Besides, although they have done outstanding and important work on this kind of structure, they haven't done further research on the effects of structural parameters on transmission efficiency and bandwidth of each channel.

To clarify the working principle of the demultiplexer with cross construction and provide an approach for the optimization of performance, in this paper, we propose a novel triple-wavelength plasmonic demultiplexer in MIM waveguide crossing with multiple side-coupled hexagonal resonators. The theoretical analysis based on the temporal coupled-mode theory reveals that wavelength demultiplexing can be realized by adjusting positions of resonators. This result is effectively proved by FDTD simulations. Moreover, FDTD simulation results illustrate that demultiplexed wavelength, transmission efficiency and bandwidth of each channel can be tuned by controlling structural parameters of the demultiplexer.

2. Model and Analysis of the Basic Component

Fig. 1 illustrates the schematic basic component. In this structure, the cavities can also be located in other positions, but due to the symmetry of the MIM waveguide crossing, we choose the configuration as shown in Fig. 1 to discuss. As shown in this figure, a pair of MIM waveguides with width w intersect to form an input port and three output channels. Two same hexagonal cavities (cavity I and cavity II) with side length L side couple to channel 1 and channel 2, respectively. g is the coupling distance between the cavities and MIM waveguide, d_1 and d_2 denote the distances of cavity I and cavity II in regard to the intersection, respectively. The material filled in the MIM waveguides is set to air with refractive index of 1, and that in the resonators is the dielectric with refractive index of n_d. The metallic material is assumed to be silver. In this model, SPPs waves are generated from the fundamental TM mode in the input port of the horizontal waveguide. Their dispersion relation is governed by the following equations [36]:

$$(\varepsilon_m k_d) \tanh\left(\frac{w k_d}{2}\right) + \varepsilon_d k_m = 0 \tag{1}$$

$$k_{d,m} = \sqrt{\beta^2 - \varepsilon_{d,m} k_0^2} \tag{2}$$

where $\varepsilon_{d,m}$ are the permittivities of the dielectric and metal, $k_{d,m}$ are the transverse wavenumbers of SPPs in the insulator and the metal, respectively. $k_0 = 2\pi/\lambda$ denotes the free space wave vector with a wavelength λ in vacuum, $\beta = k_0 n_{eff}$ stands for the propagation constant of the SPPs wave, in which n_{eff} is the effective refractive index in MIM waveguides.

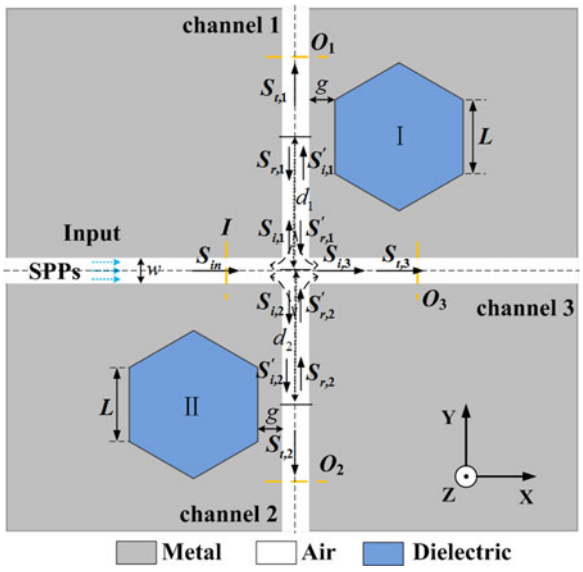

Fig. 1. Schematic diagram of the basic component with waveguide crossing and hexagonal resonators.

The transmission behaviors of SPPs in the structure can be analyzed by the temporal coupled-mode theory [37], [38]. As the schematic shows, S_{in} is the total incident amplitude, $S_{i,k}$ and $S'_{i,k}$ are incident amplitudes in each channel ($k = 1, 2, 3$), $S_{r,k}$ and $S'_{r,k}$ are reflected amplitudes, and $S_{t,k}$ are transmitted amplitudes. The amplitudes of the cavity mode in cavity I and cavity II are denoted by a and b, respectively. All the amplitudes are normalized so that their squared magnitudes correspond to modal powers. When the total incident wave reaches the intersection, due to lack of confinement in the direction perpendicular to the wave propagation, the power will be almost uniformly split into four branches [27], [31]. As a result, the incident amplitudes in each channel can be expressed as [27]

$$S_{i,1} = S_{i,2} = S_{i,3} \approx \frac{1}{2} S_{in}. \tag{3}$$

For channel 1 and channel 2, the side-coupled resonators can serve as reflectors. When the wavelength of the incident wave is close to the resonance wavelength, especially when the resonance condition is satisfied, they will be mostly reflected back. The resonance wavelength λ_m of a single hexagonal cavity is given in [19]

$$\lambda_m = \frac{(6L)\mathrm{Re}(N_{eff})}{m - \eta/2\pi} \tag{4}$$

where L is side length of cavity; $\mathrm{Re}(N_{eff})$ is the real part of the effective refractive index in the cavity, which depends mainly on the refractive index of dielectric in the cavity; m is a positive integer corresponding to the order of resonance mode; and η stands for the total phase difference caused by the corners of hexagonal cavity. We are concerned first with the temporal evolution of amplitudes

in channel 1, as follows:

$$S'_{i,1} = e^{-jd_1\beta_{spp}} S_{i,1} \tag{5}$$

$$\frac{da}{dt} = (j\omega_0 - k_0 - k_e)\, a + \sqrt{k_e} e^{j\theta} S'_{i,1} \tag{6}$$

$$S_{t,1} = S'_{i,1} - \sqrt{k_e} e^{-j\theta} a \tag{7}$$

$$S_{r,1} = -\sqrt{k_e} e^{-j\theta} a \tag{8}$$

$$S'_{r,1} = e^{-jd_1\beta_{spp}} S_{r,1}. \tag{9}$$

When S_{in} has an $e^{j\omega t}$ dependence on time, the amplitude of cavity mode can be derived as

$$a = \frac{\sqrt{k_e}}{j(\omega - \omega_0) + k_o + k_e} e^{j\theta} e^{-jd_1\beta_{spp}} S_{i,1} \tag{10}$$

where ω_0, θ, k_o and k_e are resonance frequency of the resonant cavity, the phase difference that occurs on the cavity-waveguide coupling, the decay rates caused by intrinsic loss in the cavity, and cavity-waveguide coupling loss, respectively. According to (5)–(10), the transmitted and reflected waves in channel 1 can be deduced as

$$S_{t,1} = \frac{j(\omega - \omega_0) + k_o}{j(\omega - \omega_0) + k_o + k_e} e^{-jd_1\beta_{spp}} S_{i,1} \tag{11}$$

$$S'_{r,1} = -\frac{k_e}{j(\omega - \omega_0) + k_o + k_e} e^{-jd_1\beta_{spp}} S_{i,1}. \tag{12}$$

Next, a part of $S'_{r,1}$ and $S'_{r,2}$ will flow into channel 3, and they are going to act on $S_{i,3}$. Considering the symmetry of the MIM waveguide crossing, the transmission behavior in channel 2 is similar to that in channel 1. Thus, the transmitted amplitude $S_{t,3}$ can be expressed as

$$\begin{aligned} S_{t,3} &= S_{i,3} + \frac{1}{2} S'_{r,1} + \frac{1}{2} S'_{r,2} \\ &= S_{i,3} - \left(\frac{1}{2} \frac{k_e}{j(\omega - \omega_0) + k_o + k_e} \right) e^{-j\varphi_1} S_{i,1} - \left(\frac{1}{2} \frac{k_e}{j(\omega - \omega_0) + k_o + k_e} \right) e^{-j\varphi_2} S_{i,2} \end{aligned} \tag{13}$$

where $\varphi_1 = 2d_1\beta_{spp} + \varphi_r = 4\pi d_1 n_{eff}/\lambda + \varphi_r$, $\varphi_2 = 2d_2\beta_{spp} + \varphi_r = 4\pi d_2 n_{eff}/\lambda + \varphi_r$ represent the accumulated phase differences of $S'_{r,1}$ and $S'_{r,2}$ on $S_{i,3}$, φ_r is the phase that shifted in the intersection. According to (3), (11), and (13), we can deduce the transmission efficiencies in the three channels

$$T_1 = T_2 = \left| \frac{S_{t,1,2}}{S_{in}} \right|^2 = \frac{1}{4} \frac{(\omega - \omega_0)^2 + k_o^2}{(\omega - \omega_0)^2 + (k_o + k_e)^2} \tag{14}$$

$$\begin{aligned} T_3 = \left| \frac{S_{t,3}}{S_{in}} \right|^2 &= \frac{1}{4} + \frac{1}{8} \frac{k_e^2 [1 + \cos(\varphi_1 - \varphi_2)]}{(\omega - \omega_0)^2 + (k_o + k_e)^2} \\ &+ \frac{1}{2} \frac{k_e (\omega - \omega_0) \sin[(\varphi_1 + \varphi_2)/2] \cos[(\varphi_1 - \varphi_2)/2]}{(\omega - \omega_0)^2 + (k_o + k_e)^2} \\ &- \frac{1}{2} \frac{k_e (k_e + k_o) \cos[(\varphi_1 + \varphi_2)/2] \cos[(\varphi_1 - \varphi_2)/2]}{(\omega - \omega_0)^2 + (k_o + k_e)^2}, \end{aligned} \tag{15}$$

As we can see from (14), when $\omega = \omega_0$, T_1 and T_2 will meet the minimum values. Equation (15) demonstrates that T_3 depends mainly on the phase terms φ_1 and φ_2 which are directly determined by the distances d_1 and d_2. When $\varphi_1, \varphi_2 = (2n+1)\pi$ ($n = 0, 1, 2\ldots$) (odd times π) under the resonance condition $\omega = \omega_0$, T_3 possesses the largest value T_{3max}. However, T_3 meets the smallest

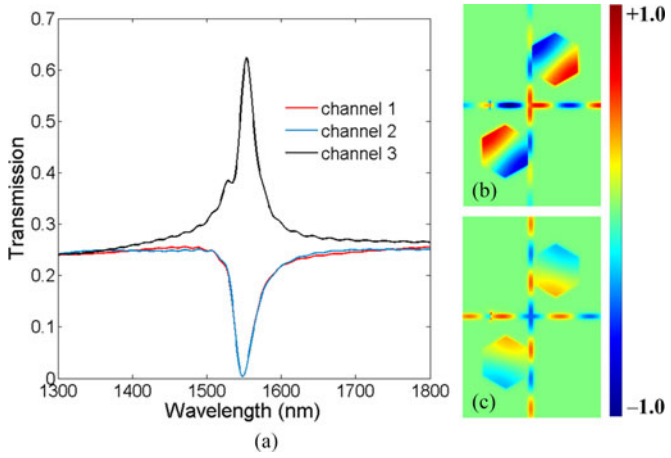

Fig. 2. (a) Transmission spectra of the basic component, where $L = 450$ nm, $w = 50$ nm, $g = 20$ nm, $d_1 = d_2 = 800$ nm, and $n_d = 1$. Field distributions of $|H_z|$ of the structure with incident wavelengths of (b) 1553.5 nm and (c) 1500 nm, respectively.

value $T_{3\min}$ if $\varphi_1, \varphi_2 = 2n\pi$ (even times π). $T_{3\max}$ and $T_{3\min}$ can be simplified as

$$T_{3\max} = \frac{1}{4} + \frac{1}{4}\frac{k_e^2}{(k_o + k_e)^2} + \frac{1}{2}\frac{k_e(k_e + k_o)}{(k_o + k_e)^2} \tag{16}$$

$$T_{3\min} = \frac{1}{4} + \frac{1}{4}\frac{k_e^2}{(k_o + k_e)^2} - \frac{1}{2}\frac{k_e(k_e + k_o)}{(k_o + k_e)^2}. \tag{17}$$

Moreover, when $\varphi_1 = (2n+1)\pi$, $\varphi_2 = 2n\pi$ (or $\varphi_1 = 2n\pi$, $\varphi_2 = (2n+1)\pi$), T_3 takes a relative minimum 1/4. In addition, from (15), we find that T_3 possesses the identical value with respect to φ_1 and φ_2 at the phase interval $\Delta\varphi = 2n\pi$, thus the period of distance $\Delta D = \lambda/2n_{eff}$ can be deduced. That is to say, if d_1 or d_2 is changed by $n \bullet \lambda/2n_{eff}$, T_3 will take the same value. The ΔD has meaning not only to the analysis of the basic component, but also to the design of the demultiplexer, and we will discuss it in the latter section again. As analyzed above, we can control the value of T_3 by adjusting the phase terms φ_1 and φ_2 as analyzed above, i.e., by changing the distances d_1 and d_2.

3. Simulations and Discussions

We take 2-D FDTD simulation to verify the aforementioned analysis. The perfectly matched layer (PML) absorbing boundary condition is utilized in our structure. To guarantee sufficient convergence of numerical simulations, the spatial and temporal steps are set to $\Delta x = \Delta y = 5$ nm and $\Delta t = \Delta x/2c$ (c is velocity of light in vacuum) [10]. In our simulations, the frequency-dependent permittivity of silver is provided by Lorentz-Drude model [15].

First of all, these parameters of the structure are set to $L = 450$ nm, $w = 50$ nm, $g = 20$ nm, and $n_d = 1$. Since n_{eff} is about 1.45 around the wavelength of 1550 nm [25], we set $d_1 = d_2 = 800$ nm to satisfy φ_1 and φ_2 are approximately equal to 3π (regarding $\varphi_1, \varphi_2 = (2n+1)\pi$, n needs to start from 1 to maintain the edges of cavities a sufficient gap apart from the edges of the horizontal waveguide). Four power monitors are placed at the locations I and O_k ($k = 1, 2, 3$) to record the total incident power P_{in} and each transmitted power $P_{t,k}$. The transmission is defined to be $T_k = P_{t,k}/P_{in}$. Fig. 2(a) shows the transmission spectra of the three channels. From the figure, we can see that a peak locates on the transmission spectrum of channel 3 at $\lambda = 1553.5$ nm, and two similar valleys on the spectra of channel 1 and channel 2. This result is shown to be consistent with the theoretical analysis in Section 2. The full width at half maximum (FWHM) of the peak is 26.8 nm and the corresponding transmission is 62.38%. It implies that a favourable band-pass filtering function is realized. The field distributions of $|H_z|$ with the incident wavelengths $\lambda = 1553.5$ nm and 1500 nm are shown in

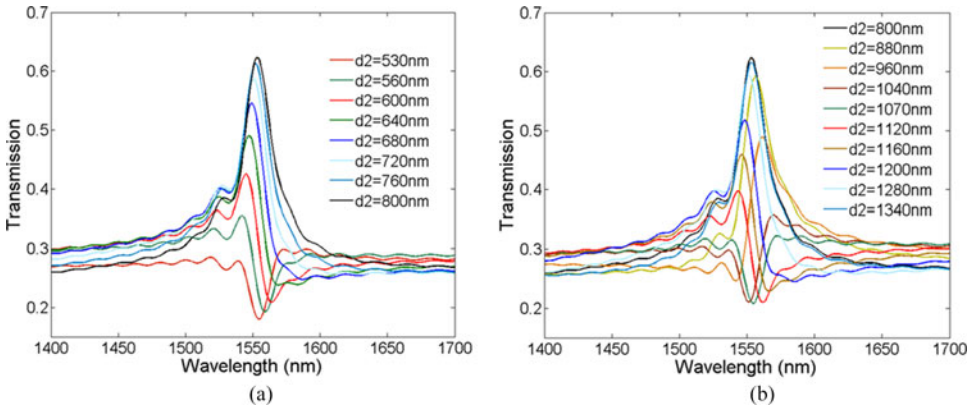

Fig. 3. Transmission spectra of channel 3 when cavity I be fixed to $d_1 = 800$ nm and then (a) shifting d_2 from 530 nm to 800 nm and (b) shifting d_2 from 800 nm to 1340 nm.

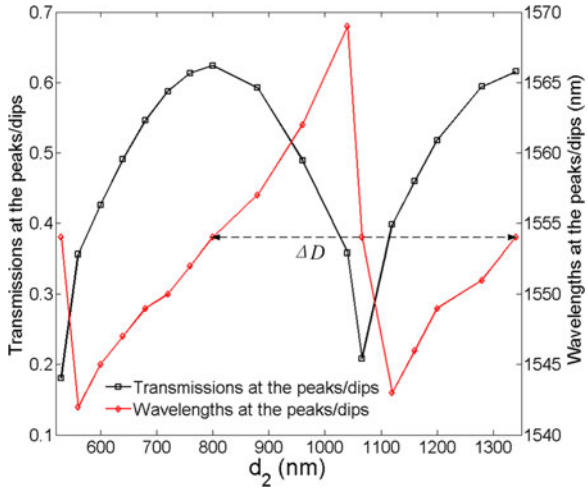

Fig. 4. Variation tendency of the transmissions (the black curve) and wavelengths (the red curve) at each peak or dip versus d_2, where $L = 450$ nm, $g = 20$ nm, $w = 50$ nm, $n_d = 1$, and $d_1 = 800$ nm.

Fig. 2(b) and (c), respectively. As can be observed from the two pictures, the harmonic standing waves are formed in the hexagonal cavities when $\lambda = 1553.5$ nm, and a majority of energy is transported to channel 3 but barely to channel 1 and channel 2. In contrast, for injecting wavelength 1500 nm, the energy is almost transmitted equivalently to each channel, whereas rarely to the cavities. The field distributions are also in agreement with the theoretical analysis.

In order to clearly illustrate the effect of the distances d_1 and d_2 on the transmission of channel 3, we fix cavity I at the position $d_1 = 800$ nm, namely φ_1 is fixed to about 3π, then move cavity II from 530 nm to 1340 nm in nonuniform intervals to change φ_2. Fig. 3 shows the transmission spectra of channel 3 for all cases. As can be seen from Fig. 3(a) and (b), with adjusting d_2 from 530 nm to 1340 nm, the transmission at peak or dip changes periodically. This variation is depicted in Fig. 4 (the black curve). In addition, when d_2 equal to 530 nm and 1070 nm, it is found that two nearly symmetric dips with transmissions of 18.3% and 20.86% appear on the corresponding spectra. This is because that when $d_2 = 530$ nm and 1070 nm, φ_2 is approximately equal to 2π and 4π; thus, T_3 takes the relative minima. On the contrary, when $d_2 = 800$ nm and 1340 nm, two highest peaks with transmission of 62.38% and 61.56% are generated in the corresponding spectra. This can be interpreted as $d_2 = 800$ nm and 1340 nm, resulting in φ_2 equal to about 3π and 5π, respectively, thus T_3 takes the largest values. Here, the period of distance can be obtained as $\Delta D = 540$ nm, which is agree well with the theoretical value (536 nm). In Fig. 4(a), it can also be observed that

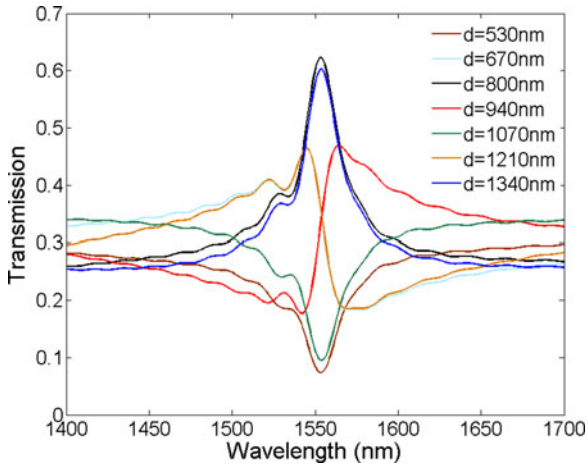

Fig. 5. Transmission spectra of channel 3 for different d, where $L = 450$ nm, $g = 20$ nm, $w = 50$ nm, and $n_d = 1$.

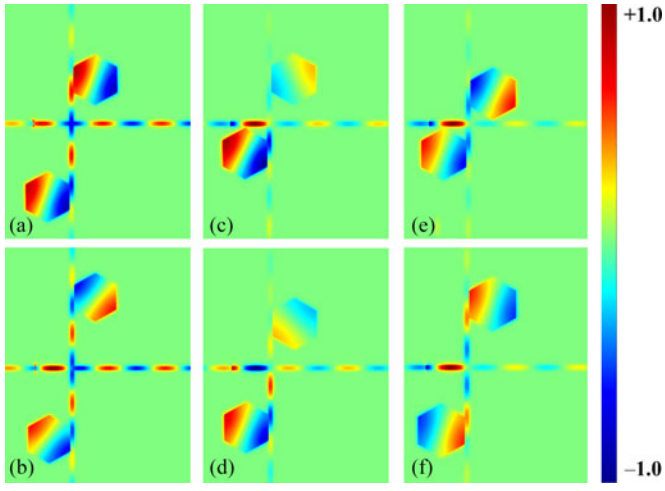

Fig. 6. Field distributions of $|H_z|$ of the structure with incident wavelength of $\lambda = 1553.5$ nm, where (a) $d_1 = 800$ nm, $d_2 = 1340$ nm; (b) $d_1 = d_2 = 1340$ nm=; (c) $d_1 = 800$ nm, $d_2 = 530$ nm; (d) $d_1 = 800$ nm, $d_2 = 1070$ nm; (e) $d_1 = d_2 = 530$ nm; and (f) $d_1 = d_2 = 1070$ nm, respectively.

the transmitted-peak and transmitted-dip wavelength changes periodically as d_2 is altered from 530 nm to 1340 nm. This phenomenon can be understood by the formula $4\pi d_2 n_{eff}/\lambda + \varphi_r = (2n + 1)\pi$. With the increase of d_2, due to n is a positive integer, λ will change to satisfy the equation. This variation is illustrated in Fig. 4 (the red curve).

Successively, remaining other parameters invariable, we put $d_1 = d_2 = d$ and then move the two cavities simultaneously from 530 nm to 1340 nm, which means that $\varphi_1 = \varphi_2 = \varphi$. Fig. 5 depicts some of these transmission spectra as an example to display the tendency. As can be observed from this figure, two highest peaks corresponding to the largest values of T_3 appear on the transmission spectra with $d = 800$ nm ($\varphi \approx 3\pi$) and $d = 1340$ nm ($\varphi \approx 5\pi$), their values are 62.38% and 60.33%, respectively. Whereas two lowest dips corresponding to the smallest values of T_3 appear on the spectra with $d = 530$ nm ($\varphi \approx 2\pi$) and $d = 1070$ nm ($\varphi \approx 4\pi$), their values are 7.43% and 9.55%, respectively. This result is in conformity with the theoretical analysis. Moreover, field distributions of $|H_z|$ for the above cases are shown in Fig. 6. It can be found that when illuminating a monochromatic light with wavelength 1553.5 nm, most of the energy is transported to the channel 3 as $d_1 = 800$ nm, $d_2 = 1340$ nm, and $d_1 = d_2 = 1340$ nm; whereas a small number as $d_1 = 800$ nm, $d_2 =$

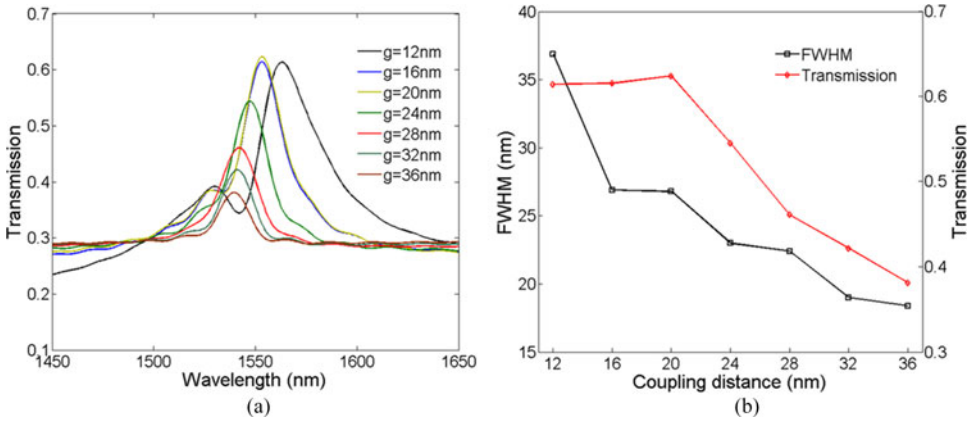

Fig. 7. (a) Transmission spectra of the structure for different coupling distances, where $L = 450$ nm, $w = 50$ nm, $d = 800$ nm, and $n_d = 1$. (b) FWHM and transmission of the peaks as a function of the coupling distances.

530 nm, and $d_1 = 800$ nm, $d_2 = 1070$ nm; and even fewer as $d_1 = d_2 = 530$ nm, and $d_1 = d_2 = 1070$ nm. These filed distributions are well consistent with the transmission spectra in Figs. 3 and 5.

Then, we investigate the effects of structural parameters on transmission characteristics by simulations. Here, according to the above analysis, we set $d_1 = d_2 = d$. In order to analyze the impact of coupling distance on the FWHM and transmission efficiency, coupling distance g is varied from 12 nm to 36 nm with an interval of 4 nm, while other parameters are fixed to $L = 450$ nm, $w = 50$ nm, $n_d = 1$, $d = 800$ nm. The transmission spectra of the structure for different coupling distances are drawn in Fig. 7(a). It shows that transmitted-peak wavelength is slightly influenced by the coupling distance. Fig. 7(b) illustrates the correlation of the FWHM and transmission peak with respect to coupling distance. As shown in Fig. 7(b), the transmission peak first increases and then decreases as the coupling distance increases, and it takes the largest value 62.38% when $d =$ 20 nm. In contrast, the FWHM monotonically decreases with the increase of coupling distance, and it can be as low as 18.4 nm with the cost of transmission efficiency. Therefore, by setting proper coupling distance, we can obtain a narrower linewidth and higher transmission efficiency.

Moreover, we explore the relationships between the transmission characteristics and side length of resonators. With fixed parameters $w = 50$ nm, $g = 20$ nm, $n_d = 1$, the side length is changed from 375 nm to 465 nm with a step of 15 nm. According to the previous analysis, the cavities with different side lengths need to find optimal positions d to take the maximum transmission efficiencies. By simulations, Fig. 8 provides the optimal distances d and periods of distance $\triangle D$ as a function of side lengths. Therefore, the transmission spectra of the structure for each side length under the optimal distance d are drawn in Fig. 9(a). As can be observed from Fig. 9(a), the side length has little little effect on the FWHM and transmission efficiency of the peak. However, the transmitted-peak wavelength has a red shift with the increase of side length. Fig. 9(b) illustrates a linear relationship between the transmitted-peak wavelength and side length. Thus, we can tune filtered wavelength by changing side length of cavities.

Furthermore, we investigate the impacts of the refractive index n_d on the transmission characteristics. Similar to the previous study, under the optimal distances d, we acquire the transmission spectra for different refractive indexes n_d from 1.0 to 1.24 with a step of 0.04. Here, other parameters L, w and g are fixed to 375 nm, 50 nm and 20 nm, respectively. As shown in Fig. 10(a), the transmission value of peak increases with the increase of the refractive index n_d, whereas the bandwidth of the peak is broadened slightly while increasing n_d. Fig. 10(b) shows a linear relationship between the transmitted-peak wavelength and refractive index n_d. Accordingly, we can also tune the filtered wavelength by changing dielectric medium filled in the cavities.

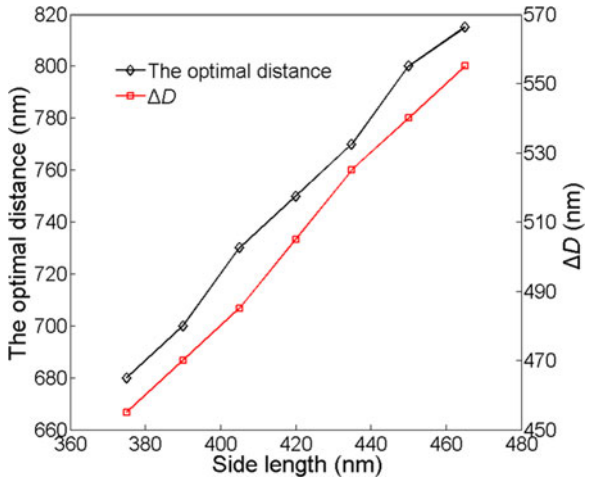

Fig. 8. Optimal distances and periods $\triangle D$ as a function of side lengths.

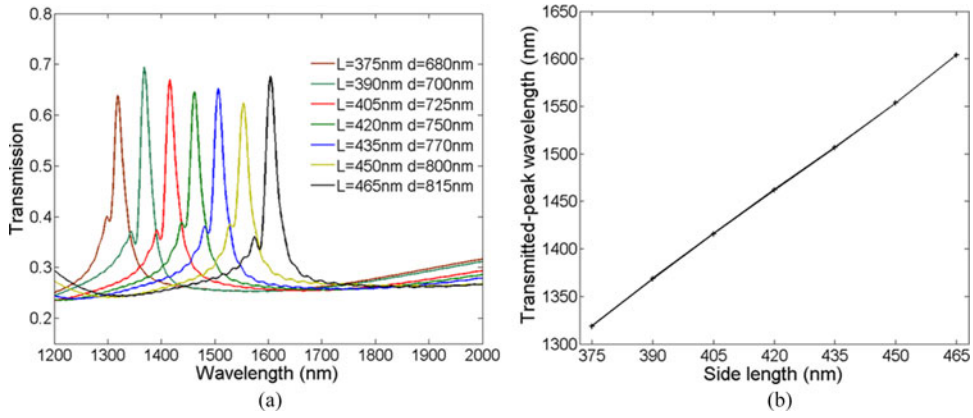

Fig. 9. (a) Transmission spectra of the structure for different side lengths under the optimal distances d, where $g = 20$ nm, $w = 50$ nm, and $n_d = 1$. (b) Transmitted-peak wavelengths as a function of side lengths.

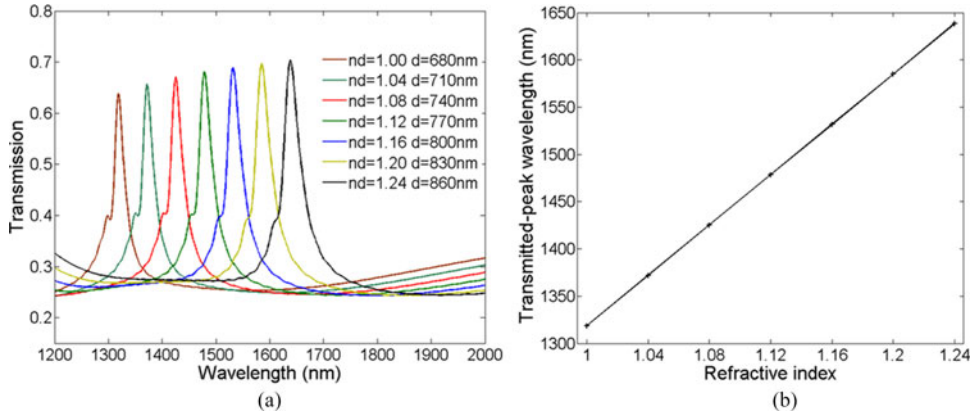

Fig. 10. (a) Transmission spectra of the structure for different refractive indexes n_d and relative distances, where $L = 375$ nm, $g = 20$ nm, and $w = 50$ nm. (b) Wavelengths at the peaks as a function of the refractive indexes n_d.

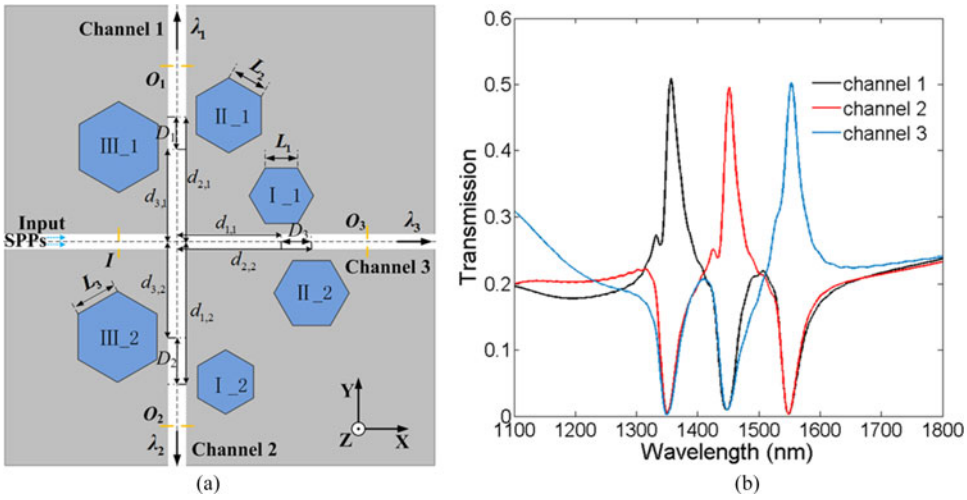

Fig. 11. (a) Schematic diagram of the proposed triple-wavelength plasmonic demultiplexer. (b) Transmission spectra of the three channels.

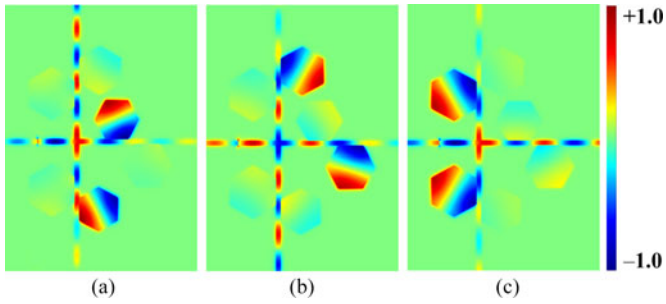

Fig. 12. Field distributions of $|H_z|$ of the triple-wavelength demultiplexer with incident wavelength of (a) 1353.5 nm, (b) 1450.5 nm, and (c) 1553.5 nm, respectively.

4. Design of a Triple-Wavelength Demultiplexer

In order to realize triple-wavelength demultiplexing, a plasmonic structure is designed which is shown in Fig. 11(a). Cavities I_1, I_2, II_1, II_2, III_1, and III_2 represent three pairs of hexagonal resonant cavities with side lengths L_k (k = 1, 2, 3). D_k denote the separations between adjacent cavities, $d_{k,1}$, $d_{k,2}$ stand for the position of each cavity. The side lengths of these cavities are chosen as L_1 = 386 nm, L_2 = 416 nm, and L_3 = 450 nm, other parameters w, g, n_d are set to 50 nm, 20 nm, 1, respectively. In order to weaken the interference between adjacent cavities and minimize the size of the configuration as possible, combining with the previous discussions, here we set $d_{1,1}$, $d_{1,2}$, $d_{2,1}$, $d_{2,2}$, $d_{3,1}$, and $d_{3,2}$ to 690 nm, 1160 nm, 1240 nm, 1240 nm, 800 nm, and 800 nm, respectively. In this way, the separations D_1, D_2, D_3 are greater than 250 nm, and the spaces between the edges of adjacent cavities are ensured over 100 nm. Therefore, the interference between adjacent cavities can be ignored [36]. Fig. 11(b) shows the transmission spectra of the three channels. As shown in the figure, a transmission peak appears on each spectrum accompanies with two transmission valleys. The transmitted-peak wavelengths of the channel 1, channel 2, and channel 3 are 1353.5 nm, 1450.5 nm, and 1553.5 nm, respectively. The transmission efficiencies of the three peaks 50.95%, 49.6%, 50.34% are obtained with corresponding FWHM 28.4 nm, 25.4 nm and 26.5 nm, respectively. It means that the structure can effectively demultiplex three different wavelengths into each channel. Moreover, the lowest transmission linewidth is smaller than the result given by [36] (about 30 nm) with similar transmission efficiency. According to the relationships between the transmission characteristics and structural parameters, the demultiplexed wavelength can be tuned by adjusting side length of resonators or changing the dielectric medium

filled in the cavities. Moreover, Fig. 12(a)–(c) depict the field distributions of $|H_z|$ with incident wavelengths 1353.5 nm, 1450.5 nm, and 1553.5 nm, in which we find that the monochromatic light with a specific wavelength can only pass through the corresponding channel but be prevented from the other two channels. The field distributions are in good agreement with the transmission spectra in Fig. 11(b).

5. Conclusion

In summary, we have proposed and numerically studied a triple-wavelength demultiplexer in MIM waveguide crossing with multiple side-coupled hexagonal resonators. The working principle and transmission characteristics of this structure are analyzed by the temporal coupled-mode theory and FDTD method. FDTD simulation results demonstrate that demultiplexed wavelength can be tuned by controlling side length of the resonators and dielectric filled in the resonators. Furthermore, the transmission efficiency and bandwidth of each channel can be manipulated by changing coupling distance. By choosing appropriate geometric parameters, the transmission efficiency higher than 49.6% with the FWHM down to 25.4 nm are realized. The proposed plasmonic demultiplexer may have some significance for constructing highly integrated optical circuits and complex waveguide networks.

References

[1] D. K. Gramotnev and S. I. Bozhevolnyi, "Plasmonics beyond the diffraction limit," *Nature Photon.*, vol. 4, no. 2, pp. 83–91, Feb. 2010.
[2] H. Ditlbacher, J. R. Krenn, G. Schider, A. Leitner, and F. R. Aussenegg, "Two-dimensional optics with surface plasmon polaritons," *Appl. Phys. Lett.*, vol. 81, no. 10, pp. 1762–1764, Sep. 2002.
[3] X. Ren, G. Guo, Y. Huang, Z. Wang, P. Zhang, and G. Guo, "Interference of surface plasmon polaritons controlled by the phase of incident light," *Appl. Phys. Lett.*, vol. 92, no. 17, Apr. 2008, Art. no. 171106.
[4] X. Luo and L. Yan, "Surface plasmon polaritons and its applications," *IEEE Photon. J.*, vol. 4, no. 2, pp. 590–595, Apr. 2012.
[5] W. L. Barnes, A. Dereux, and T. W. Ebbesen, "Surface plasmon subwavelength optics," *Nature*, vol. 424, no. 14, pp. 824–830, Aug. 2003.
[6] E. Ozbay, "Plasmonics: Merging photonics and electronics at nanoscale dimensions," *Science*, vol. 311, no. 5758, pp. 189–193, Jan. 2006.
[7] R. F. Oulton *et al.*, "Plasmon lasers at deep subwavelength scale," *Nature*, vol. 461, no. 7264, pp. 629–632, Oct. 2009.
[8] X. Lin and X. Huang, "Tooth-shaped plasmonic waveguide filters with nanometeric sizes," *Opt. Lett.*, vol. 33, no. 23, pp. 2874–2876, Dec. 2008.
[9] A. Drezet, D. Koller, A. Hohenau, A. Leitner, F. R. Aussenegg, and J. R. Krenn, "Plasmonic crystal demultiplexer and multiports," *Nano Lett.*, vol. 7, no. 6, pp. 1697–1700, May 2007.
[10] B. Wang and G. Wang, "Surface plasmon polariton propagation in nanoscale metal gap waveguides," *Opt. Lett.*, vol. 29, no. 17, pp. 1992–1994, Sep. 2004.
[11] Y. Zhou and B. Yang, "A 4-way wavelength demultiplexer based on the plasmonic broadband slow wave system," *Opt. Exp.*, vol. 22, no. 18, pp. 21589–21599, Sep. 2014.
[12] G. Xiao, X. Wang, and Z. Zhou, "Propagation properties of symmetric surface slasmon polaritons mode in Au/Al_2O_3/Au waveguide," *IEEE Photon. Technol. Lett.*, vol. 24, no. 8, pp. 628–630, Apr. 2012.
[13] J. A. Dionne, L. A. Sweatlock, H. A. Atwater, and A. Polman, "Plasmon slot waveguides: Towards chip-scale propagation with subwavelength- scale localization," *Phys. Rev. B*, vol. 73, no. 3, Jan. 2006, Art. no. 035407.
[14] J. Tao, X. Huang, X. Lin, Q. Zhang, and X. Jin, "A narrow-band subwavelength plasmonic waveguide filter with asymmetrical multiple-teeth-shaped structure," *Opt. Exp.*, vol. 17, no. 16, pp. 13989–13994, Aug. 2009.
[15] T. Wang, X. Wen, C. Yin, and H. Wang, "The transmission characteristics of surface plasmon polaritons in ring resonator," *Opt. Exp.*, vol. 17, no. 26, pp. 24096–24101, Dec. 2009.
[16] G. Wang, H. Lu, and X. Liu, "Gain-assisted trapping of light in tapered plasmonic waveguide," *Opt. Lett.*, vol. 38, no. 4, pp. 558–560, Feb. 2013.
[17] H. Lu, X. Liu, L. Wang, Y. Gong, and D. Mao, "Ultrafast all-optical switching in nanoplasmonic waveguide with Kerr nonlinear resonator," *Opt. Exp.*, vol. 19, no. 4, pp. 2910–2915, Feb. 2011.
[18] L. Xu, S. Wang, and L. Wu, "Refractive index sensing based on plasmonic waveguide side coupled with bilaterally located double cavities," *IEEE Trans. Nanotechnol.*, vol. 13, no. 5, pp. 875–880, Sep. 2014.
[19] Y. Xie, Y. Huang, W. Zhao, W. Xu, and C. He, "A novel plasmonic sensor based on metal-insulator-metal waveguide with side-coupled hexagonal cavity," *IEEE Photon. J.*, vol. 7, no. 2, Apr. 2015, Art. no. 4800612.
[20] M. A. Ayad, S. S. A. Obayya, and M. A. Swillam, "Submicron 1xN ultra wideband MIM plasmonic power splitters," *J. Lightw. Technol.*, vol. 32, no. 9, pp. 1814–1820, May 2014.
[21] Y. D. Wu, "High transmission efficiency wavelength division multiplexer based on metal-insulator-metal plasmonic waveguides," *J. Lightw. Technol.*, vol. 32, no. 24, pp. 4844–4848, Dec. 2014.

[22] H. Lu, X. Liu, Y. Gong, D. Mao, and L. Wang, "Enhancement of transmission efficiency of nanoplasmonic wavelength demultiplexer based on channel drop filters and reflection nanocavities," *Opt. Exp.*, vol. 19, no. 14, pp. 12885–12890, Jul. 2011.
[23] F. Hu, H. Yi, and Z. Zhou, "Wavelength demultiplexing structure based on arrayed plasmonic slot cavities," *Opt. Lett.*, vol. 36, no. 8, pp. 1500–1502, Apr. 2011.
[24] H. Liu, Y. Gao, B. Zhu, G. Ren, and S. Jian, "A T-shaped high resolution plasmonic demultiplexer based on perturbations of two nanoresonators," *Opt. Commun.*, vol. 334, pp. 164–169, Aug. 2014.
[25] S. Xiao and N. A. Mortensen, "Resonant-tunnelling-assisted crossing for subwavelength plasmonic slot waveguides," *Opt. Exp.*, vol. 16, no. 19, pp. 14997–15005, Sep. 2008.
[26] G. Veronis, Ş. E. Kocabaş, D. A. Miller, and S. Fan, "Modeling of plasmonic waveguide components and networks," *J. Comput. Theor. Nanosci.*, vol. 6, no. 8, pp. 1808–1826, Aug. 2009.
[27] E. Feigenbaum, S. P. Burgos, and H. A. Atwater, "Programming of inhomogeneous resonant guided wave networks," *Opt. Exp.*, vol. 18, no. 25, pp. 25584–25595, Dec. 2010.
[28] E. Feigenbaum and H. A. Atwater, "Resonant guided wave networks," *Phys. Rev. Lett.*, vol. 104, no. 14, Apr. 2010, Art. no. 147402.
[29] Z. Guo, J. Duan, and Y. Yang, "On-line multicast scheduling with bounded congestion in fat-tree data center networks," *IEEE J. Sel. Areas Commun.*, vol. 32, no. 1, pp. 102–115, Jan. 2014.
[30] Y. Xie *et al.*, "Formal worst-case analysis of crosstalk noise in mesh-based optical networks-on-chip," *IEEE Trans. Very Large Scale Integr. Syst.*, vol. 21, no. 10, pp. 1823–1836, Aug. 2013.
[31] E. Feigenbaum and M. Orenstein, "Modeling of complementary (void) plasmon waveguiding," *J. Lightw. Technol.*, vol. 25, no. 9, pp. 2547–2562, Sep. 2007.
[32] J. Liu, G. Fang, H. Zhao, Y. Zhang, and S. Liu, "Plasmon flow control at gap waveguide junctions using square ring resonators," *J. Phys. D: Appl. Phys.*, vol. 43, no. 5, Jan. 2010, Art. no. 055103.
[33] M. A. Bavil, L. Gao, and X. Sun, "A compact nanoplasmonics filter and intersection structure based on utilizing a slot cavity and a Fabry-Perot resonator," *Plasmonics*, vol. 8, no. 2, pp. 631–636, Sep. 2012.
[34] K. Wen, L. Yan, Y. Hu, L. Chen, and L. Lei, "A plasmonic wavelength-selected intersection structure," *Plasmonics*, vol. 9, no. 3, pp. 685–690, Feb. 2014.
[35] H. Lu, X. Liu, L. Wang, D. Mao, and Y. Gong, "Nanoplasmonic triple-wavelength demultiplexers in two-dimensional metallic waveguides," *Appl. Phys. B*, vol. 103, no. 4, pp. 877–881, May 2011.
[36] F. Lu, Z. Wang, K. Li, and A. Xu, "A plasmonic triple-wavelength demultiplexing structure based on a MIM waveguide with side-coupled nanodisk cavities," *IEEE Trans. Nanotechnol.*, vol. 12, no. 6, pp. 1185–1190, Nov. 2013.
[37] Y. Akahane, T. Asano, B. S. Song, and S. Noda, "Fine-tuned high-Q photonic-crystal nanocavity," *Opt. Exp.*, vol. 13, no. 4, pp. 1202–1214, Feb. 2005.
[38] Q. Li, T. Wang, Y. Su, M. Yan, and M. Qiu, "Coupled mode theory analysis of mode-splitting in coupled cavity system," *Opt. Exp.*, vol. 18, no. 8, pp. 8367–8382, Apr. 2010.